INTERNATIONAL JOURNAL FOR NUMERICAL METHODS IN FLUIDS
Int. J. Numer. Meth. Fluids 2000; **33**: 203–222

The capturing of free surfaces in incompressible multi-fluid flows

Dartzi Pan*,[1] and Chih-Hao Chang

Institute of Aeronautics and Astronautics, National Cheng Kung University, Tainan, Taiwan, Republic of China

SUMMARY

By treating it as a contact discontinuity in the density field, a free surface between two immiscible fluids can be automatically 'captured' by the enforcement of conservation laws. A surface-capturing method of this kind requires no special tracking or fitting treatment for the free surface, thereby offering the advantage of algorithm simplicity over the surface-tracking or the surface-fitting method. A surface-capturing method based on a new multi-fluid incompressible Navier–Stokes formulation is developed. It is applied to a variety of free-surface flows, including the Rayleigh–Taylor instability problem, the ship waves around a Wigley hull and a model bubble-rising problem to demonstrate the validity and versatility of the present method. Copyright © 2000 John Wiley & Sons, Ltd.

KEY WORDS: free-surface capturing; incompressible multi-fluid flows

1. INTRODUCTION

The flow field with a deformable free surface is common in engineering applications. An understanding of the dynamics of the free surface is of practical importance in problems such as the thermocapillary convection in crystal growth, the liquid sloshing in tanks and the flow and heat transfer in mold filling processes. The computation of such flows remains a challenge because the free surface is a boundary of the fluid domain and it must be determined as part of the flow solution. Generally, there are three approaches to compute such flows, namely, the surface-fitting method, the surface-tracking method and the surface-capturing method. The surface-fitting method [1–3] treats the free surface as a free-floating grid boundary. This is very efficient for simple free surfaces but its validity is limited by the skewness of the resulting grid. The surface-tracking method [4–6] tracks the free surface by a separate marker function in a Lagrangian manner. The shape of the free surface is then reconstructed from the

* Correspondence to: Institute of Aeronautics and Astronautics, National Cheng Kung University, Tainan, Taiwan 70101, Republic of China. Tel.: +886 6 2757575, Ext. 63658; fax: +886 6 2389940.
[1] E-mail: dpan@mail.ncku.edu.tw

Received March 1999
Revised August 1999

distribution of the market function. These methods are powerful and popular, however, the tracking and the reconstruction of the free surface remain complicated and difficult in these methods, especially in three dimensions.

The surface-capturing method [7–9] views a free surface as a contact discontinuity in the density field. Similar to the shock-capturing method for compressible flow algorithms, a surface-capturing method automatically captures the free surface by the enforcement of conservation laws. No special modeling for the free surface is necessary, thereby eliminating the complexity of the surface-fitting and surface-tracking procedures. Kelecy and Pletcher [7] discretized the variable density incompressible Navier–Stokes equations using total variation diminishing (TVD) schemes to capture free surfaces in closed containers. However, their method was applied only to the two-fluid system in closed containers and the numerical smearing of the free surface was quite severe. In this paper, a new multi-fluid incompressible Navier–Stokes formulation [8,9] is developed using the artificial compressibility. An MUSCL-type TVD finite volume method is employed for the capturing of the free surfaces. To control the numerical smearing, a slope modification (SM) method [10], originally developed for essentially non-oscillatory (ENO) schemes, is modified and adapted to introduce a proper amount of artificial compression. The resulting TVD/SM scheme is applied to a variety of free-surface problems to demonstrate its validity and versatility, including the Rayleigh–Taylor instability problem, the surface waves around a Wigley hull and a model bubble-rising problem.

2. GOVERNING EQUATIONS

Consider the system of multiple immiscible, non-reacting and incompressible fluids in a control volume, as for example an air–oil–water system. Assume that the mass density and molecular viscosity are constant for all fluids. Assume that the interface between two fluids is so thin that it can be viewed as a discontinuity in the density field without interfacial molecular diffusion or phase change. The surface tension is neglected and the flow is assumed laminar.

Let the incompressibility of the flow be treated by the artificial compressibility method. Add a virtual time term with the understanding that the true flow equations will be recovered when the virtual time term is driven to zero. The integral form of the Navier–Stokes equations can be written as

$$\frac{\partial}{\partial \tau}\int_{CV} Q \, \mathrm{d}V = -\left(I_d \frac{\partial}{\partial t}\int_{CV} Q \, \mathrm{d}V + \oint_{CS} F_n \, \mathrm{d}S - \int_{CV} H \, \mathrm{d}V \right) \tag{1}$$

where τ is the virtual time, t is the physical time, Q is the mass-averaged conserved variables in the control volume CV, I_d is a unity matrix except for a zero entry for the continuity equation (the first row), F_n is the flux function through the control surface CS with unit normal vector $\hat{\boldsymbol{n}}$, and H is the source term representing body forces. For the m-fluid system, the definitions are

$$Q=\begin{pmatrix} p/\beta \\ \rho u \\ \rho v \\ \rho w \\ \varphi_1 \\ \vdots \\ \varphi_{m-1} \end{pmatrix}, \quad F_n=\begin{pmatrix} U_n \\ \rho uU+pn_x \\ \rho vU+pn_y \\ \rho wU+pn_z \\ \varphi_1 U \\ \vdots \\ \varphi_{m-1}U \end{pmatrix} - \frac{\mu}{Re}\begin{pmatrix} 0 \\ \hat{\boldsymbol{n}}\cdot(\nabla u+\partial\vec{\boldsymbol{v}}/\partial x) \\ \hat{\boldsymbol{n}}\cdot(\nabla v+\partial\vec{\boldsymbol{v}}/\partial y) \\ \hat{\boldsymbol{n}}\cdot(\nabla w+\partial\vec{\boldsymbol{v}}/\partial z) \\ 0 \\ \vdots \\ 0 \end{pmatrix}, \quad H=\frac{\rho}{Fr^2}\begin{pmatrix} 0 \\ g_x \\ g_y \\ g_z \\ 0 \\ \vdots \\ 0 \end{pmatrix}$$

$$\vec{\boldsymbol{v}}=u\hat{\boldsymbol{i}}+v\hat{\boldsymbol{j}}+w\hat{\boldsymbol{k}}, \qquad \hat{\boldsymbol{n}}=n_x\hat{\boldsymbol{i}}+n_y\hat{\boldsymbol{j}}+n_z\hat{\boldsymbol{k}}, \qquad \vec{\boldsymbol{g}}=g_x\hat{\boldsymbol{i}}+g_y\hat{\boldsymbol{j}}+g_z\hat{\boldsymbol{k}}, \qquad U=(\vec{\boldsymbol{v}}-\vec{\boldsymbol{v}}_b)\cdot\hat{\boldsymbol{n}},$$
$$U_n=\vec{\boldsymbol{v}}\cdot\hat{\boldsymbol{n}}, \qquad I_d=\mathrm{diag}(0,1,1,1,1,\ldots,1) \tag{2}$$

where p is the averaged pressure in the control volume CV, β is the artificial compressibility coefficient, ρ is the average mass density of the fluid in CV, φ_i is the volume fraction of fluid i in CV, $\vec{\boldsymbol{v}}$ is the mass-averaged velocity in CV, $\vec{\boldsymbol{v}}_b$ is the velocity of the control surface CS, μ is the average molecular viscosity of the fluid in CV, $\vec{\boldsymbol{g}}$ is the vector of gravitation, $Re=(UL\rho/\mu)_{\mathrm{ref}}$ is the reference Reynolds number and $Fr=(U/\sqrt{gL})_{\mathrm{ref}}$ is the reference Froude number. The average mass density of the fluid is related to the volume fraction by

$$\rho=\sum_{i=1}^{m-1}(\rho_i\varphi_i)+\left(1-\sum_{i=1}^{m-1}\varphi_i\right)\rho_m=\sum_{i=1}^{m-1}(a_i\varphi_i)+b \tag{3}$$

where ρ_i is the mass density of fluid I, $a_i=(\rho_i-\rho_m)$ and $b=\rho_m$ are constants. Normally the mth fluid is the lightest fluid in the system. All variables are normalized by the appropriate reference quantities, for example, ρ by ρ_{ref}, $\vec{\boldsymbol{v}}_b$ and $\vec{\boldsymbol{v}}_b$ by U_{ref}, p by $\rho_{\mathrm{ref}}U_{\mathrm{ref}}^2$, length by L_{ref}, time by $L_{\mathrm{ref}}/U_{\mathrm{ref}}$, etc.

The inviscid flux Jacobian matrix A for the m-fluid system has been derived [9] as

$$A=\begin{pmatrix}
0 & n_x/\rho & n_y/\rho & n_z/\rho & (-a_1/\rho)U_n & \cdots & (-a_i/\rho)U_n & \cdots & (-a_{m-1}/\rho)U_n \\
\beta n_x & U+un_x & un_y & un_z & -ua_1U_n & \cdots & -ua_iU_n & \cdots & -ua_{m-1}U_n \\
\beta n_y & vn_x & U+vn_y & vn_z & -va_1U_n & \cdots & -va_iU_n & \cdots & -va_{m-1}U_n \\
\beta n_z & wn_x & wn_y & U+wn_z & -wa_1U_n & \cdots & -wa_iU_n & \cdots & -wa_{m-1}U_n \\
0 & (\varphi_1/\rho)n_x & (\varphi_1/\rho)n_y & (\varphi_1/\rho)n_z & U-(\varphi_1/\rho)a_1U_n & \cdots & -(\varphi_1/\rho)a_iU_n & \cdots & -(\varphi_1/\rho)a_{m-1}U_n \\
\vdots & \vdots & \vdots & \vdots & \vdots & \ddots & \vdots & \vdots & \vdots \\
0 & (\varphi_i/\rho)n_x & (\varphi_i/\rho)n_y & (\varphi_i/\rho)n_z & -(\varphi_i/\rho)a_1U_n & \cdots & U-(\varphi_i/\rho)a_iU_n & \cdots & -(\varphi_i/\rho)a_{m-1}U_n \\
\vdots & \vdots & \vdots & \vdots & \vdots & \cdots & \vdots & \ddots & \vdots \\
0 & (\varphi_{m-1}/\rho)n_x & (\varphi_{m-1}/\rho)n_y & (\varphi_{m-1}/\rho)n_z & -(\varphi_{m-1}/\rho)a_1U_n & \cdots & -(\varphi_{m-1}/\rho)a_iU_n & \cdots & U-(\varphi_{m-1}/\rho)a_{m-1}U_n
\end{pmatrix} \tag{4}$$

The eigenvalues of A are

$$\lambda^-=U'-C, \qquad \lambda^+=U'+C, \qquad \lambda^0=U \tag{5}$$

with

$$U' = \frac{1}{2}\left(U + \frac{b}{\rho} U_n\right), \qquad C = \sqrt{(U')^2 + \frac{\beta}{\rho}}$$

where C is the artificial speed of sound, λ^- and λ^+ are the eigenvalues that are always negative and positive respectively, the multiplicity of λ^0 is $m+1$ for the m-fluid system. A linearly independent set of eigenvectors can be chosen as done in Pan and Chakravarthy [11]. Since the eigenvalues of A are all real, the inviscid part of Equation (1) is hyperbolic in τ. The eigensystem of A and Roe's approximate Riemann solver are given in Chang [9]. The Roe's state variables are

$$q^{\mathrm{Roe}} = \frac{\sqrt{\rho^{\mathrm{R}}} q^{\mathrm{R}} + \sqrt{\rho^{\mathrm{L}}} q^{\mathrm{L}}}{\sqrt{\rho^{\mathrm{R}}} + \sqrt{\rho^{\mathrm{L}}}}, \qquad \rho^{\mathrm{Roe}} = \sqrt{\rho^{\mathrm{R}} \rho^{\mathrm{L}}} \tag{6}$$

where the superscripts 'R' and 'L' indicate the right and left states; q^{Roe} represents the Roe state of u or v or w. The Roe state for volume fraction is

$$\phi_i^{\mathrm{Roe}} = \frac{\sqrt{\rho^{\mathrm{R}}} \varphi_i^{\mathrm{L}} + \sqrt{\rho^{\mathrm{L}}} \varphi_i^{\mathrm{R}}}{\sqrt{\rho^{\mathrm{R}}} + \sqrt{\rho^{\mathrm{L}}}} \tag{7}$$

One can verify that a density discontinuity with equal pressure and normal velocity on both sides satisfies the jump condition, provided that the artificial compressibility β is constant.

3. FINITE VOLUME FORMULATION

The computational domain should be large enough to include the free surface of interest and the fluids on both sides of the free surface. Using a structured grid system, the semi-discretized form of Equation (1) can be written for a computational cell as

$$\left(\frac{\partial (QV)}{\partial \tau}\right)_{i,j,k} = -\left(I_d \frac{\partial (QV)}{\partial t} + \sum_1^6 F_n \Delta S - (HV)\right)_{i,j,k} = -\left(I_d \frac{\partial (QV)}{\partial t} + RH\right)_{i,j,k} \tag{8}$$

where (i, j, k) are the integer indices indicating the cell center, and the summation of flux functions F_n is done over the six cell faces surrounding cell (i, j, k). Neglecting the cell indices for simplicity and using the first-order Euler implicit for τ, the time discretization for Equation (8) can be written as

$$\left(\frac{V}{\Delta \tau} + I_d \frac{c_1 V}{\Delta t} + I_\theta \frac{\partial RH}{\partial Q}\right)(Q^{s+1} - Q^s)$$

$$= -\left(I_d \frac{[c_1(Q^s - Q^n) - c_2(Q^n - Q^{n-1})]V}{\Delta t} + I_\theta RH^s + (I - I_\theta) RH^n\right) = \mathrm{Res}^s \tag{9}$$

where $I_\theta = \mathrm{diag}(1, \theta, \ldots, \theta)$ is a diagonal matrix. The superscript n is the time index for t; s is the sub-iteration index for τ; c_1, c_2 and θ are the constants to determine the time accuracy for t. When the sub-iteration in s converges, the right-hand side of Equation (9) is the second-order accurate backward time differencing with ($c_1 = 1.5$, $c_2 = 0.5$, $\theta = 1$), the second-order accurate trapezoidal rule with ($c_1 = 1$, $c_2 = 0$, $\theta = 0.5$), and the first-order accurate Euler implicit scheme with ($c_1 = 1$, $c_2 = 0$, $\theta = 1$).

4. TOTAL VARIATION DIMINISHING/SLOPE MODIFICATION (TVD/SM)

To compute the numerical flux function F_n at the cell face, a locally one-dimensional Riemann problem is solved at the cell interfaces using Roe's approximate solver [8,9]. The left and right states of φ_i, u, v, w and p at the cell interface are obtained by the modified Osher–Chakravarthy interpolation [12], which can be written as

$$
\begin{aligned}
Q^{\mathrm{L}}_{j+1/2} &= Q_j + \zeta\left[(\xi+\eta\chi)\Delta Q_{j+1/2} + \frac{1}{\xi}(1-\eta\chi)\Delta Q_{j-1/2}\right] \\
Q^{\mathrm{R}}_{j-1/2} &= Q_j - \zeta\left[(\xi-\eta\chi)\Delta Q_{j+1/2} + \frac{1}{\xi}(1+\eta\chi)\Delta Q_{j-1/2}\right] \\
\xi &= \frac{\ell_j + \ell_{j-1}}{\ell_j + \ell_{j+1}}, \qquad \eta = \frac{2\ell_j}{\ell_{j+1} + \ell_j}, \qquad \zeta = \frac{\ell_j}{\ell_{j+1} + 2\ell_j + \ell_{j-1}} \\
\Delta Q_{j+1/2} &= Q_{j+1} - Q_j, \qquad \Delta Q_{j-1/2} = Q_j - Q_{j-1}
\end{aligned}
\tag{10}
$$

where ℓ_j represents the mean cell width in the j-direction (defined as the length connecting the centers of two opposite cell faces), χ is a weighting factor for the stencil points. For a model one-dimensional hyperbolic equation with a smooth wave profile on uniform grids, Equation (10) yields third-order spatial accuracy with $\chi = \frac{1}{3}$, which is used throughout this paper. A TVD slope limiter is designed to control the numerical oscillation by replacing the variable differences in Equation (10) with their limited values defined as

$$
\begin{aligned}
\tilde{\Delta} Q_{j+1/2} &= \mathrm{minmod}\{\Delta Q_{j+1/2}, \varepsilon^{\mathrm{R}}_{j-1/2}\Delta Q_{j-1/2}\} \\
\tilde{\Delta} Q_{j-1/2} &= \mathrm{minmod}\{\Delta Q_{j-1/2}, \varepsilon^{\mathrm{L}}_{j+1/2}\Delta Q_{j+1/2}\} \\
\varepsilon^{\mathrm{R}}_{j-1/2} &= \frac{\xi - \zeta(1+\eta\chi)}{\xi\zeta(\xi-\eta\chi)}, \qquad \varepsilon^{\mathrm{L}}_{j+1/2} = \frac{\xi - \xi\zeta(\xi+\eta\chi)}{\zeta(1-\eta\chi)} \\
\mathrm{minmod}\{a, b\} &= \begin{cases} 0 & \text{if } ab \le 0 \\ \mathrm{sgn}(a)\,\min(|a|, |b|) & \text{if } ab \ge 0 \end{cases}
\end{aligned}
\tag{11}
$$

Note that it is necessary to have different right and left limiters to obtain the TVD property. It is known that a discontinuity in φ_i traveling with the local velocity field is a linear wave, and

a TVD scheme is too diffusive for such a wave. To reduce the numerical smearing, the slope modification method [10] originally developed for equal-spaced ENO schemes is modified in this paper to add a proper amount of artificial compression to the interpolated φ_i. This is accomplished by adding a correction to the volume fraction after Equation (10) as

$$\tilde{\varphi}^{\mathrm{L}}_{j+1/2} = \varphi^{\mathrm{L}}_{j+1/2} + \delta\varphi_j, \qquad \tilde{\varphi}^{\mathrm{R}}_{j-1/2} = \varphi^{\mathrm{R}}_{j-1/2} - \delta\varphi_j$$

$$\delta\varphi_j = \mathrm{minmod}\{\vartheta_j\ \mathrm{minmod}(\varphi^{\mathrm{R}}_{j-1/2} - \varphi^{\mathrm{L}}_{j-1/2},\ \varphi^{\mathrm{R}}_{j+1/2} - \varphi^{\mathrm{L}}_{j+1/2}),$$
$$\mathrm{minmod}(\varphi_{j+1} - \varphi^{\mathrm{L}}_{j+1/2},\ \varphi^{\mathrm{R}}_{j-1/2} - \varphi_{j-1})\} \tag{12}$$

where ϑ_j is a parameter to be chosen. The amount of artificial compression is zero when $\vartheta_j = 0$ and increases as ϑ_j increases. In Yang [10] it was suggested that ϑ_j should be between 1.9 and 2.3 for ENO schemes. In the present work, a constant $\vartheta_j = 2$ is chosen after several numerical experiments.

The computation of viscous fluxes requires the velocity gradient on the cell faces. This velocity gradient is calculated by the Gauss theorem [13] using the four cell vertices and the two cell centers enclosing the particular cell face. The viscous force calculated in this way is spatially second-order accurate on uniform grids. The dynamic viscosity at the cell center is obtained by the volume averaging as

$$\mu = \sum_{i=1}^{m} \varphi_i \mu_i \tag{13}$$

where μ_i is the dynamic viscosity of fluid i.

5. IMPLICIT OPERATORS

The direct inversion of Equation (9) is still prohibitive for the present day computers. Some sort of relaxation scheme must be employed in an implicit scheme. To reduce the computational work, two simplifications are done to the implicit operator while the high-order accuracy of the explicit operators is kept unchanged. First, to reduce the bandwidth of the implicit operator, only a first-order spatial accuracy is used for the inviscid fluxes on the implicit side. Take the j-dimensional as an example, the inviscid Jacobians are chosen for simplicity as

$$\frac{\partial RH^I_j}{\partial Q_{j-1}} = -A^{+}_{j-1/2}\Delta S_{j-1/2}$$

$$\frac{\partial RH^I_j}{\partial Q_j} = A^{+}_{j-1/2}\Delta S_{j-1/2} - A^{-}_{j+1/2}\Delta S_{j+1/2}$$

$$\frac{\partial RH^I_j}{\partial Q_{j+1}} = A^{-}_{j+1/2}\Delta S_{j+1/2} \tag{14}$$

with

$$A^+ = R\Lambda^+ L, \qquad A^- = R\Lambda^- L \tag{15}$$

where Λ^+ and Λ^- are respectively the positive and negative eigenvalue matrices of A; R and L are respectively the right and left eigenvector matrices of A; and $\Delta S_{j+1/2}$ is the area of surface between cell j and $j+1$.

The second simplification of the implicit operator is to neglect the cross-derivatives of the viscous fluxes on the implicit side. Specifically, the viscous Jacobians in j direction are taken as

$$\begin{aligned}
\frac{\partial RH_j^V}{\partial Q_{j-1}} &= -\frac{\mu_{j-1/2}}{Re}\frac{2\Delta S_{j-1/2}^2}{V_j + V_{j-1}} \\
\frac{\partial RH_j^V}{\partial Q_j} &= \frac{\mu_{j-1/2}}{Re}\frac{2\Delta S_{j-1/2}^2}{V_j + V_{j-1}} + \frac{\mu_{j+1/2}}{Re}\frac{2\Delta S_{j+1/2}^2}{V_j + V_{j+1}} \\
\frac{\partial RH_j^V}{\partial Q_{j+1}} &= -\frac{\mu_{j+1/2}}{Re}\frac{2\Delta S_{j+1/2}^2}{V_j + V_{j+1}}
\end{aligned} \tag{16}$$

where V_j is the volume of cell j.

6. APPROXIMATE LU FACTORIZATION

The inversion of Equation (9) is completed iteratively by an approximate LU factorization scheme (ALU) [13]. The implicit operator is split into a diagonal matrix D, a lower triangular part L and an upper triangular part U. Then, Equation is approximately factored into

$$(D+L)D^{-1}(D+U)\Delta Q^s = \mathrm{Res}^s \tag{17}$$

which can be inverted by a two-step scheme as

$$\begin{aligned}
(D+L)\Delta Q^* &= \mathrm{Res}^s \\
(D+U)\Delta Q^{s+1} &= \mathrm{Res}^s - L\Delta Q^*
\end{aligned} \tag{18}$$

This two-step inversion is more efficient than the three-step inversion usually seen in literature. The inversion of Equation (18) requires only matrix–vector multiplication and $(m+3)\times(m+3)$ matrix inversion for an m-fluid system. However, the diagonal dominance of the implicit operator in Equation (18) requires some special attention.

Assuming a constant surface area, the operators in Equation (14) form a well-conditioned matrix if the spectra radius of $A^+_{j-1/2} - A^-_{j+1/2}$ is greater than the spectra radius of $A^+_{j-1/2}$ and $A^+_{j+1/2}$. This well conditioning is generally satisfied when the density variation in the m-fluid system is small. However, when the density differs greatly across the free surface, the

well conditioning of the implicit operator is generally lost. This can be seen by examining a model flux Jacobian matrix

$$A(q) = \begin{pmatrix} 0 & q^2 \\ 1 & 0 \end{pmatrix}$$

whose eigenvalues are $\lambda^+ = q$ and $\lambda^- = -q$. A simple derivation will show that both eigenvalues of $A^+(q_1) - A^-(q_2)$ are $0.5(q_1 + q_2)$, whose magnitude is between $|q_1|$ and $|q_2|$. Thus, when $q^{\mathrm{Roe}}_{j+1/2}$ and $q^{\mathrm{Roe}}_{j-1/2}$ differ greatly across a free surface, the diagonal dominance of the implicit operator in Equation (18) can only be achieved by using a very small $\Delta\tau$ or Δt, or equivalently a very small Courant–Friedrich–Lewy (CFL) number in τ or t. A quick fix for this problem is to replace $A^+_{j-1/2}\Delta S_{j-1/2} - A^-_{j+1/2}\Delta S_{j+1/2}$ in the diagonal term of Equation (14) by $|A|_{j-1/2}\Delta S_{j-1/2} + |A|_{j+1/2}\Delta S_{j+1/2}$. This will ensure the diagonal dominance of Equation (18) with the consequence of increasing stability and decreasing convergence rate.

7. BOUNDARY CONDITIONS

There is no special treatment required for the free surface. All boundary conditions used in the present work are originally designed for the Navier–Stokes or Euler equations. The grid lines are assumed to be normal to the grid boundary for at least one cell. This is necessary to ensure at least first-order accuracy on the boundary when simple extrapolation is used. For viscous walls the no-slip condition applies. For inviscid walls the normal velocity component on the wall is set to zero and the tangential component is extrapolated from the flow interior. The volume fraction on the wall is extrapolated from the flow interior assuming a constant distribution in the cell. The pressure on the wall is obtained form solving the momentum equation normal to the wall, including the source terms. Specially, the following equation is written for the cells adjacent to the wall:

$$\hat{\mathbf{n}}_{\mathrm{w}} \cdot \left\{ \frac{V(\rho^s \vec{\mathbf{v}}^s - \rho^n \vec{\mathbf{v}}^n)}{\Delta t} + \sum_1^6 \left[p\hat{\mathbf{n}} + \rho U \vec{\mathbf{v}} - \frac{\mu}{Re}\left(\frac{\partial v_i}{\partial x_j} + \frac{\partial v_j}{\partial x_i}\right) n_j \right] \Delta S - \frac{\rho}{Fr^2} \vec{\mathbf{g}} V \right\} = 0 \tag{19}$$

where $\hat{\mathbf{n}}_{\mathrm{w}}$ is the unit normal vector of the wall, n_j, v_j and x_j are the index notation of $\hat{\mathbf{n}}$, $\vec{\mathbf{v}}$ and position vector $\vec{\mathbf{r}}$ respectively. By using the latest value for all variables except the pressure on the wall, and using a distance-weighted averaging for the cell-face variable values, Equation (19) can be used to solve the pressure on the wall at the new iteration. The same treatment also applies to the inviscid flow. Note that the gravity is included in Equation (19). Thus the hydrostatic pressure is naturally included in the solution when Equation (19) is satisfied.

For the inflow and outflow boundaries at the far field, the grid is designed such that the gravity vector is parallel to one particular grid direction and normal to others. Then, in the directions normal to the gravity vector, the non-reflecting characteristic boundary condition [11] can be applied. For example, at the inflow boundary there is only one negative eigenvalue λ^- carrying characteristic information from the flow interior. Thus, the flow variables at the inflow boundary can be obtained by

$$\begin{pmatrix} L_{11} & L_{12} & \cdots & L_{1j} & \cdots & L_{1,m+3} \\ L_{21} & L_{22} & \cdots & L_{2j} & \cdots & L_{2m+3} \\ \vdots & \vdots & \vdots & \vdots & \vdots & \vdots \\ L_{i1} & L_{i2} & \cdots & L_{ij} & \cdots & L_{i,m+3} \\ \vdots & \vdots & \vdots & \vdots & \vdots & \vdots \\ L_{m+3,1} & L_{m+3,2} & \cdots & L_{m+3,j} & \cdots & L_{m+3,m+3} \end{pmatrix} \begin{pmatrix} q_1 \\ q_2 \\ \vdots \\ q_i \\ \vdots \\ q_{m+3} \end{pmatrix}_{\text{boundary}} = \begin{pmatrix} \sum (L_{1k}q_k)_{\text{interior}} \\ \sum (L_{2k}q_k)_{\text{free}} \\ \vdots \\ \sum (L_{ik}q_k)_{\text{free}} \\ \vdots \\ \sum (L_{m+3,k}q_k)_{\text{free}} \end{pmatrix} \tag{20}$$

where the subscript 'boundary' indicates boundary values, 'interior' indicates values extrapolated from the cell center next to the boundary and 'free' indicates the inflow free stream values. The summations are done for index $k = 1$ to $m + 3$. Equation (20) provides excellent non-reflecting boundary treatment in the present work. A similar equation can be defined for the outflow boundary where the only information coming from downstream far field is carried by λ^-. However, often it is adequate to use a simple extrapolation at the outflow boundary when the downstream boundary is far enough and the flow is fully developed.

8. NUMERICAL EXPERIMENTS

The residual vector is defined as the right-hand side of Equation (9) divided by the cell volume. Unless otherwise mentioned, the L_2 norm of both the divergence field $\nabla \cdot \vec{v}$ and the residual vector are under $1.0e-5$ for the validation cases show herein. Most computations are done on a Pentium Pro-200 PC with 128-MB memory. The compiler is the f77 under Linux. Only single precision is used. The artificial compressibility β is 10 for all cases. The quick fix on the diagonal term mentioned in Section 5 is used for all cases.

Ethier and Steinman [14] have obtained an exact solution of the incompressible Navier–Stokes equations. This solution is used to examine the spatial accuracy of the present method. The Reynolds number is 1. The constants in the solution of Either and Steinman [14] are chosen as $a = \pi/4$ and $d = \pi/2$. The flow domain is a cubic cavity $-1 \leq x, y, z \leq 1$. The trapezoidal method is first used to march one time step from $t = 0$ with $\Delta t = 0.002$. Then the flow is marched another 39 time steps using the second-order backward difference method. The computation is done using a two-fluid model with $\varphi = 0$ everywhere.

Initially, the pressure and velocity fields are specified by the analytical solution everywhere. All boundaries use the Dirichlet boundary condition. It is known that a closed domain with fixed boundary conditions is not well posed for the hyperbolic nature of the present solver. The error signal will be reflected at the boundary, and only the inherent numerical dissipation of the upwind scheme acts to damp the noisy waves. However, to assess the spatial accuracy of the flux terms, 10000 sub-iteration counts are performed to drop both L_2 norms of the divergence field and the residual vector to below $1.0e-6$. Then the pressure and velocity components are compared with the analytical solution. The L_2 norms of the error of pressure and velocity components are shown in Figure 1 for different grid spacings after 40 time steps. The order of spatial accuracy estimated from Figure 1 is about 2.2 for the pressure and 2.0 for the velocity components. This is considered satisfactory since the viscous term is only second-order accurate.

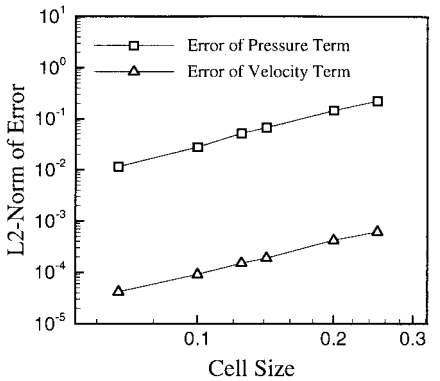

Figure 1. Order of accuracy test, Navier–Stokes equations.

The second test concerns the convection of a contact surface. Consider a one-dimensional contact surface with $\rho = 0.001$ ($\varphi = 0$) on the left and $\rho = 1$ ($\varphi = 1$) on the right. The initial position is at $x = 1$. The grid cell length is 0.1, the time step is $\Delta t = 0.02$, and the right-traveling velocity is one. This amounts to a CFL number of 20. The maximum sub-iteration count is 20. Here it should be mentioned that the allowable CFL number is extremely small without the quick fix mentioned in Section 5. Figure 2 shows the density distribution after 300 time steps. The captured free surface spans about eight cells for the TVD scheme and about four cells for the TVD/SM scheme. From now on, we define $\varphi = 0.5$ to be the location of the free surface, and the distance between $\varphi = 0.1$ and $\varphi = 0.9$ to be the captured thickness of the free surface. Figure 3 shows the time history of the captured thickness. The TVD/SM scheme maintains the thickness within two cells, while the first-order upwind scheme and the TVD-alone scheme continuously smear the discontinuity. This case shows the importance of the addition of artificial compression using the SM method.

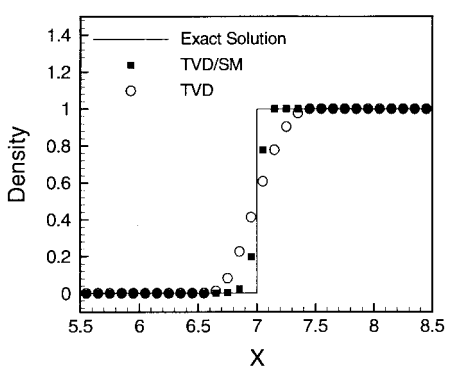

Figure 2. Traveling one-dimensional contact surface.

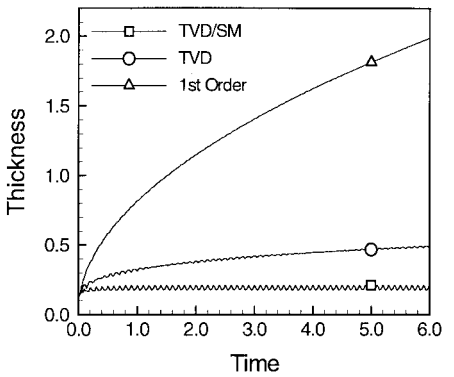

Figure 3. Thickness of the captured free surface.

The rotation of two-dimensional contact surface is examined next. In Rudman [15], several single-variable evolution equations for the fluid marker or color function are tested, including Noh and Woodward's simplified line interface calculation (SLIC) method, Hirt and Nichols' volume of fluid (VOF) method, Youngs' VOF method and the Rudman's flux-corrected transport (FCT)–VOF method. Here we compute Zalesak's problem and compare it with the results in Rudman [15]. The contact surface of the shape of a slotted circle shown in Figure 4 is rotated in a constant angular velocity. The computational domain is 4.0×4.0 and the grid is $200 \times 200 \times 1$. The diameter of the slotted circle is 50 mesh cells and the slot width is six mesh cells. Th grid resolution in the slotted region is rather poor for the present method, since generally the TVD/SM requires four cells for one discontinuity and eight cells for two. This set-up is used in Rudman; hence it is followed here. The axis of the rotation center is on (2, 2), the center of slotted circle is on (2.0, 2.75) and the angular velocity is 0.5. The time step is about 0.005, which completes one rotation in 2524 steps. The maximum sub-iteration count is 20, which is enough to keep the L_2 norm of momentum and divergence residuals under $1.0e-7$. In Figure 4, contour levels of 0.025, 0.5 and 0.975 are shown for the initial condition and the results after one rotation. The TVD result has severe smearing as expected. The TVD/SM method maintains the outer circular boundary well, however, inside the slotted region the contours of 0.025 fuse together because the lack of grid resolution as described above. Examining the results copied from Rudman in Figure 5, the results by SLIC and Hirt–Nichols' VOF methods have poor interface shapes and noisy jetsam. The best result is due to Youngs' method, in which only a small round off is found on the corner of slotted region. But Youngs' method requires a quite complicated reconstruction procedure [15], even in two dimensions. In contrast, no special reconstruction procedure is required in the present surface-capturing method. Table I shows the relative solution error defined by

$$\text{error} = \frac{\sum_{i,j} |\varphi^n_{i,j} - \varphi^e_{i,j}|}{\sum_{i,j} \varphi^0_{i,j}} \tag{21}$$

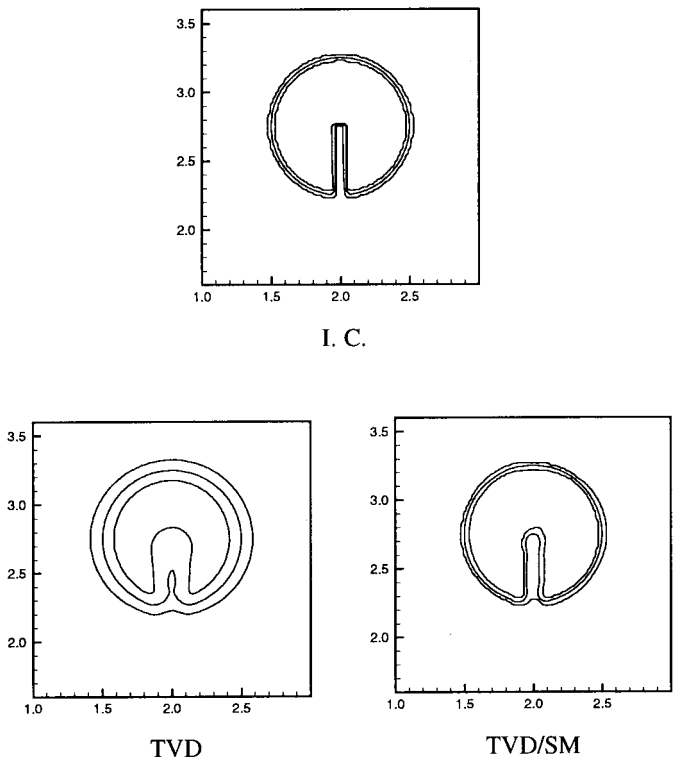

Figure 4. Volume fraction contours of Zalesak's problem by the present work, $\varphi = 0.025$, 0.5 and 0.975, $\Delta t = 4.98 \times 10^{-3}$, $t = 12.57$, second-order backward difference in time.

where φ^n is the calculated solution after n time steps, φ^e is the exact solution after n time steps and φ^0 is the initial solution. The error generated by TVD/SM method is larger than Youngs' method, about the same as FCT–VOF result, and smaller than other methods.

The next validation case is the computation of Rayleigh–Taylor instability [16,17]. When a heavy fluid is superposed over a lighter fluid in a vertical gravitational field, the interface between the two fluids is unstable. Small perturbations on the interface will be amplified, and the amplitude of the perturbation will grow with time. The computation of the initial growth rate of the instability has been used as a validation case. Since the interface will soon roll up to a mushroom-like shape, the problem serves as a good demonstration of the capability of the method to compute wave breaking.

The present work considers the two-dimensional Rayleigh–Taylor instability for a viscous incompressible two-fluid layer. The computational domain, as shown in Figure 6, is an enclosed rectangle with width L and depth D with $L/D = 1.5$ for each fluid. A uniform grid of $40 \times 120 \times 1$ is used. Following the work by Daly [17], a single wavelength perturbation is

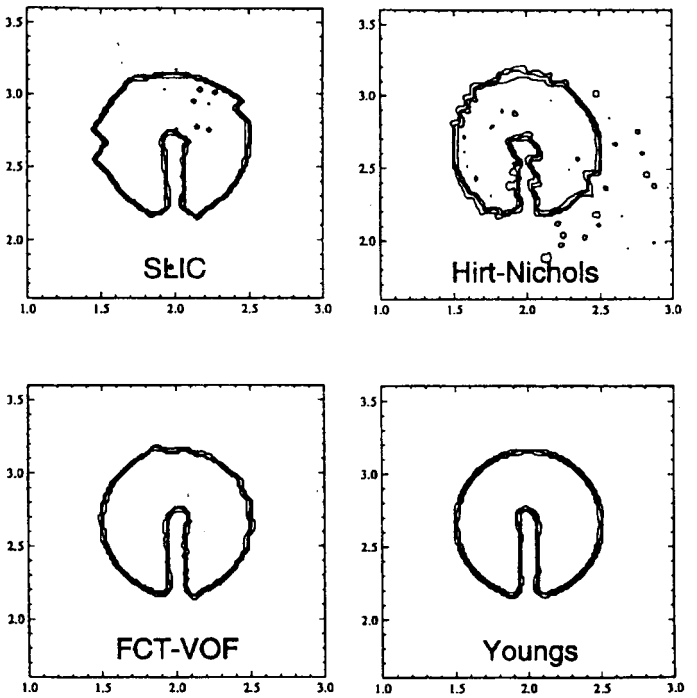

Figure 5. VOF function contours of Zalesak's problem from Rudman [15], $\varphi = 0.025$, 0.5 and 0.975, $\Delta t = 4.98 \times 10^{-3}$, $t = 12.57$.

introduced on the interface, which can be written as

$$u = \begin{cases} \dfrac{\pi A \Delta y}{2L} \sin\left(\dfrac{\pi x}{L}\right) \exp\left(\dfrac{-\pi |y|}{L}\right) & \text{as } y \geq 0 \\ -\dfrac{\pi A \Delta y}{2L} \sin\left(\dfrac{\pi x}{L}\right) \exp\left(\dfrac{-\pi |y|}{L}\right) & \text{as } y \leq 0 \end{cases}$$

$$v = \frac{\pi A \Delta y}{2L} \cos\left(\frac{\pi x}{L}\right) \exp\left(\frac{-\pi |y|}{L}\right) \tag{22}$$

where A is the perturbation amplitude, Δy is the mesh spacing in the y-direction. This velocity field corresponds to a sinusoidal perturbation of wavelength $\lambda = 2L$. The pressure field is set to hydrostatic equilibrium initially. The inviscid wall boundary condition is imposed on all sides of the boundary.

The Froude number is $Fr = 1$. The Reynolds number is $Re = 283$. The density ratio is $\rho_2/\rho_1 = 2$, where ρ_1 and ρ_2 are the fluid density of the lower and the upper layer respectively.

Table I. Relative error for Zalesak's problem from Rudman [15] and the present work.

Method	Relative error
SLIC	8.38×10^{-2}
Hirt–Nichols' VOF	9.62×10^{-2}
FCT–VOF	3.29×10^{-2}
Young's VOF	1.09×10^{-2}
TVD	1.543×10^{-2}
TVD/SM	3.292×10^{-2}

The perturbation amplitude A is set to be 1.0. The computed evolution of the interface is shown in Figure 7 by contour lines of $\varphi = 0.1$, $\varphi = 0.9$ and $\varphi = 0.5$. It can be seen that the lighter fluid rises along the left boundary, and heavy fluid sinks along the right boundary. In the early stage when the movement of the interface is small and linear, the displacement of the interface is seen to be symmetric. As time evolution continues, the interface rolls up to a mushroom shape. The flow becomes highly non-linear.

According to the linear theory, the viscosity has an important effect on the growth rate of Rayleigh–Taylor instability. As pointed out by Chandrasekhar [18], for a given wavelength of perturbation and Reynolds number, there exists a single positive exponential growth rate for this type of instability. This growth rate of instability can be estimated by measuring the displacement of the interface on the wall. In this work, a small perturbation with amplitude $A = 0.1$ is selected to delay the non-linear effect and help maintaining the linear behavior of the solution during the transient. The computed time history of the displacement of the interface

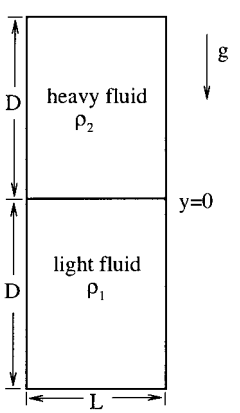

Figure 6. Definition of Rayleigh–Taylor instability problem.

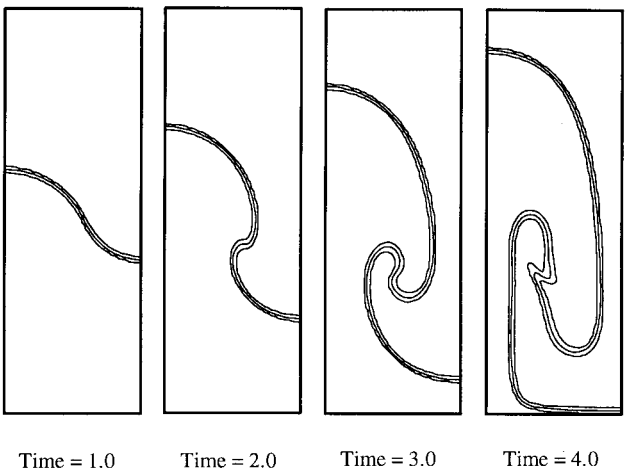

Figure 7. Rayleigh–Taylor instability, $Fr = 1$, $Re = 283$, $\rho_2/\rho_1 = 2$, $\varphi = 0.1$, 0.5 and 0.9, TVD/SM scheme, $\vartheta = 2$.

on the wall is shown in Figure 8. The amplitude of instability is defined as the average of the absolute displacement of the left and right interface. After the stable modes of the disturbance in the initial transient have decayed away, the natural logarithm of the amplitude of instability becomes linear with time. The slope of the linear region gives the exponential growth rate n^* of the corresponding Reynolds number. Based on the time interval of 0.2 and 0.5, the

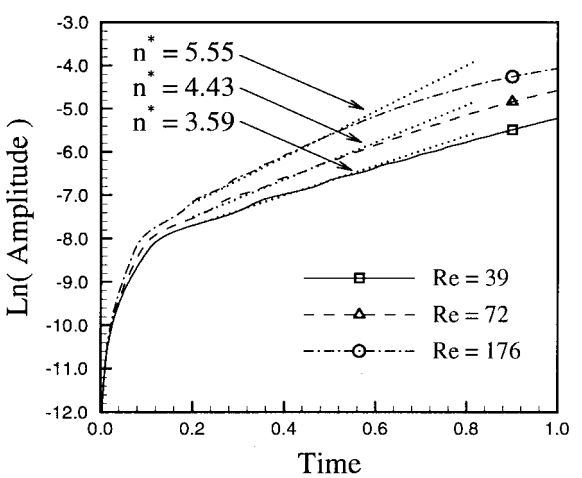

Figure 8. Estimation of linear growth rate of Rayleigh–Taylor instability, $Fr = 1$, $\rho_2/\rho_1 = 2$, $A = 0.1$.

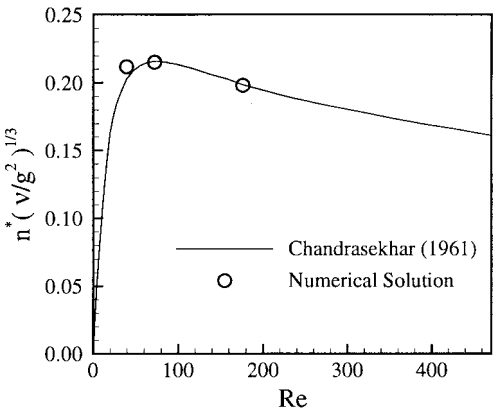

Figure 9. Non-dimensional perturbation growth rate versus Reynolds number for Rayleigh–Taylor instability, $Fr = 1$, $\rho_2/\rho_1 = 2$.

computed exponential growth rate is 3.59, 4.43 and 5.55 for Reynolds number $Re = 39$, 72 and 176 respectively. The values given by Daly [17] are 3.6, 4.5 and 5.6 for the same Reynolds numbers. A comparison of the computed growth rate with the prediction by linear analysis of Chandrasekhar [18] is given in Figure 9. The numerical results show good agreement with the theoretical curve.

The next example shown here is for the surface waves around a Wigley ship hull. This is an example of the free surface flows in open field with far-field inflow and outflow boundaries. Only inviscid results are obtained to save computer resources. A grid of $110 \times 37 \times 31$ cells is used with 50 cells along the hull with a symmetry plane in y. The ship length is one and the computational domain is ten lengths upstream, 20 lengths downstream, one length on the side and three lengths below the ship hull. A free surface is specified at the inflow boundary. The air:water density ratio is taken to be 1:100 to reduce the numerical stiffness. Our experience indicates that when the density ratio is greater than 1:100, the light fluid (air) has only an insignificant effect on the dynamics of the heavy fluid (water). Figures 10 and 11 show respectively for $Fr = 0.25$ and $Fr = 0.316$ the detailed wave profiles, from bow to stern along the hull, comparing with the experiment [19]. Figure 12 shows the free surface ($\varphi = 0.5$) elevation for $Fr = 0.316$, amplified three times for clarity. Note that the wave height is very small compared with the ship length. The minimum grid spacing is $2.5\text{e}-3$, which is about $\frac{1}{6}$ to $\frac{1}{8}$ of the wave height. The large grid stretching and the high-density ratio make the problem very stiff and amenable to small and slow oscillations. The wave profiles in Figures 10 and 11 are averaged over a long time period, and the maximum amplitude of oscillation is $1.0\text{e}-3$, which is less than the minimum grid spacing. The L_2 norm of the divergence field for both cases is under $1.0\text{e}-6$, but the L_2 norm of residual is $1.8\text{e}-5$ for the $Fr = 0.25$ case, and $2.3\text{e}-5$ for the $Fr = 0.316$ case.

The last example is a two-dimensional bubble-rising problem modeled by a three-fluid system of density ratio 0.01:0.5:1. For convenience, the fluids are tagged as air, oil and water.

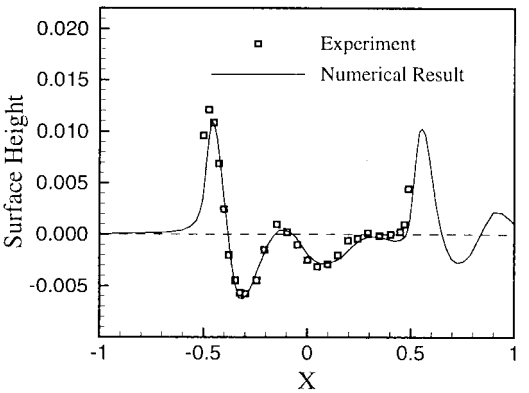

Figure 10. Wave height along Wigley hull, $Fr = 0.25$.

Initially, a circular bubble of oil is immersed in the water that occupies the lower half of a closed container with air above it. At $t = 0$, the oil bubble starts rising in the water. The computational domain is a 3×3.5 rectangular in non-dimensional length. The initial depth of water is 2.5. The diameter of the oil bubble is 1.0 and center of the bubble is located 1.0 below the water surface. The Froude number is $Fr = 1.0$. It is assumed for convenience that the kinematic viscosity of water and oil are the same, and the Reynolds number based on the diameter of the oil bubble is 200. It is known that for such a viscous system, the surface tension and capillary forces will be very important. However, the surface tension effect has not been included in the present method yet. Thus, it is expected that the quantitative information deduced from this example would not be physically correct. This example serves only as a demonstration of a three-fluid computation.

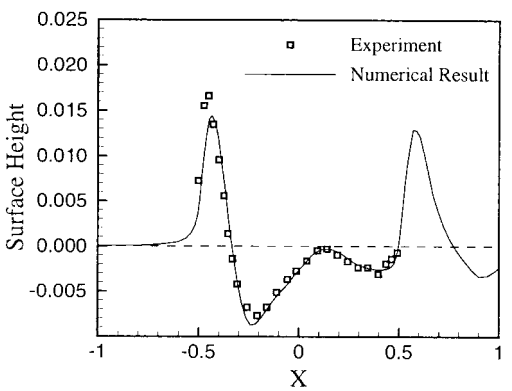

Figure 11. Wave height along Wigley hull, $Fr = 0.316$.

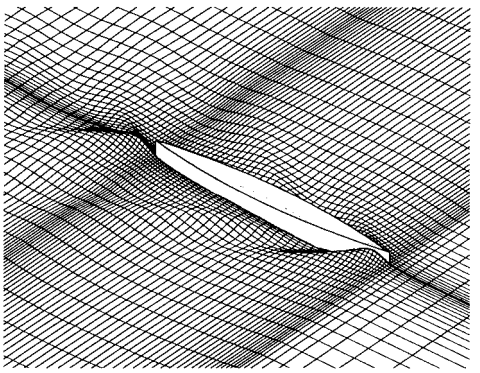

Figure 12. Surface waves amplified three times, $\varphi = 0.5$, $Fr = 0.316$.

A uniformly distributed grid of $120 \times 140 \times 1$ is used for this computation. The flow field is in hydrostatic equilibrium initially and all the boundaries assume the no-slip condition. Figure 13 shows the time sequence of a bubble rising. The volume fraction contour lines of 0.9, 0.5 and 0.1 are shown for air and oil. The bubble accelerates upward from its original position due to the buoyancy force. The water–air surface swell upward in the region above the rising bubble. Two circulating vortices gradually form at the two sides of the bubble. The upward velocity at the bottom flattens the lower half of the bubble at around $t = 1.5$, and the bubble deforms into a kidney shape at around $t = 2.0$. The bubble continues to deform as it approaches the water–air interface because the upper portion of the bubble experiences less buoyancy and is being pushed aside by the lower half of the bubble. This elongates the oil bubble to both sides. At $t = 4.0$, the oil bubble almost hits the water–air surface. There are waves on the water–air surface due to the water flow beneath the surface. Two vortices in the air can also be seen.

It should be kept in mind that if the surface tension was present; the deformation of the bubble shape and the water–air surface will be much less significant than the results shown here. Since the surface tension effect has not been included, it is not very meaningful to show further computations. Nonetheless, this computation has shown that the present method is capable of handling a multi-fluid and multi-interface situation.

9. CONCLUSIONS

A surface-capturing method based on a new incompressible multi-fluid formulation has been validated through a variety of free-surface computations. The method captures a free surface by the enforcement of conservation laws. No special modeling of the free surface is required. This offers the advantage of algorithm simplicity when compared with the surface-fitting or the surface-tracking method. The TVD/SM method is capable of capturing a free surface within two cells ($0.1 \leq \varphi \leq 0.9$) with minimum numerical oscillation. The test on Zalesak's problem

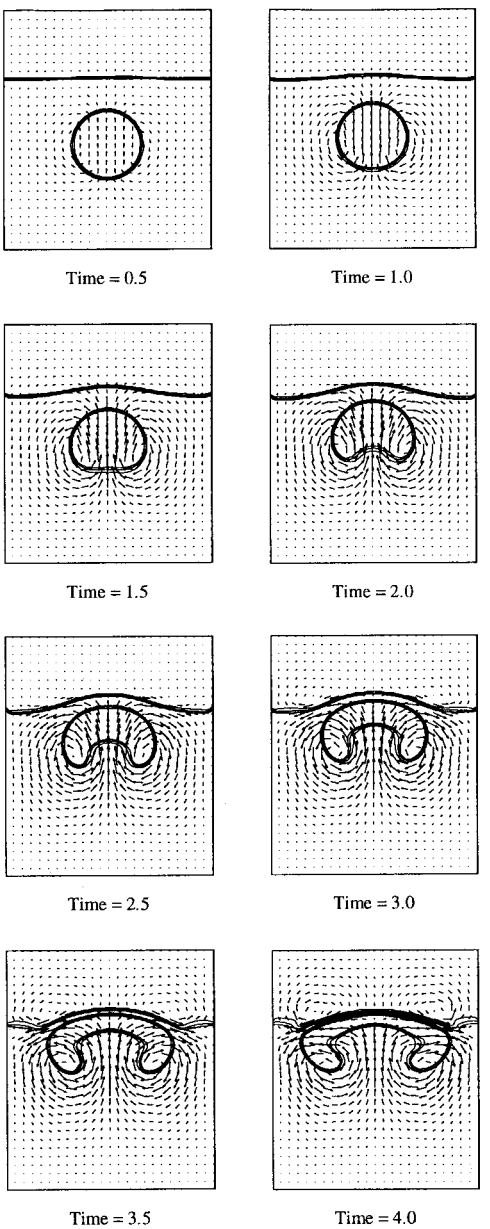

Figure 13. Time evolution of rising bubble problem, ρ_{water}:ρ_{oil}:ρ_{air} = 1:0.5:0.01, $Fr = 1.0$, $Re = 200$, $\varphi_{oil} = 0.1$, 0.5 and 0.9 (bubble), $\varphi_{air} = 0.1$, 0.5 and 0.9, overlapped with velocity vector plot.

indicated that the present method outperforms most of the existing surface-tracking method. Two types of free surface flows are successfully demonstrated in the present paper, namely, those inside a closed container, such as the Rayleigh–Taylor instability problem, and those in the open field with far-field inflow and outflow boundaries, such as ship wave problems. The computation of a model bubble-rising problem has indicated the applicability of the present method to a multi-fluid and multi-interface situation.

ACKNOWLEDGMENTS

This work is partially supported by the National Science Council under grants NSC86-2212-E006-058 and NSC88-2212-E006-076.

REFERENCES

1. Farmer J, Martinelli L, Jameson A. A fast multigrid method for solving incompressible hydrodynamic problems with free surfaces. *AIAA Journal* 1994; **32**(6): 1175–1182.
2. Liu H, Ikehata M. Computation of free surface waves around an arbitrary body by a Navier–Stokes solver using the psuedocompressibility technique. *International Journal for Numerical Methods in Fluids* 1994; **19**: 395–413.
3. Liou BH, Martinelli L, Jameson A. A fully implicit multigrid driven algorithm for time-resolved non-linear free-surface flow on unstructured grids. *ASME Fluid Engineering Division Conference* 1996; **238**: 349–354.
4. Okamoto T, Kawahara M. 3D sloshing analysis by an arbitrary Lagrangian–Eulerian finite element method. *International Journal for Computational Fluid Dynamics* 1997; **8**: 129–146.
5. Ushijima S. Three-dimensional arbitrary Lagrangian–Eulerian numerical prediction method for non-linear free surface oscillation. *International Journal for Numerical Methods in Fluids* 1998; **26**: 605–623.
6. Pan D, Yang YS, Chang CH. Computation of internal flow with free surfaces using artificial compressibility. *Numerical Heat Transfer B* 1998; **33**: 119–134.
7. Kelecy FJ, Pletcher RH. The development of a free surface capturing approach for multidimensional free surface flows in closed container. *Journal of Computational Physics* 1997; **138**: 939–980.
8. Pan D, Chang CH, Chao M-J. Research efforts on computational aerodynamics and computational hydrodynamics with free surfaces. (Invited) Proceedings of the 39th Conference on Aeronautics and Astronautics, Tainan, Taiwan, ROC, December, 1997; 3–14.
9. Chang CH. The development of a multi-fluid surface-capturing method for the computation of incompressible free surface flows. PhD thesis, Institute of Aeronautics and Astronautics, National Cheng Kung University, June, 1998.
10. Yang H. An artificial compression method for ENO schemes: the slope modification method. *Journal of Computational Physics* 1990; **89**: 125–160.
11. Pan D, Chakravarthy SR. Unified formulation for incompressible flows. AIAA Paper 89-0122, Reno, January, 1989.
12. Lu PJ, Pan D, Yeh DY. Transonic flutter suppression using active acoustic excitations. *AIAA Journal* 1995; **33**(4): 694–702.
13. Pan D, Cheng JC. Upwind finite volume Navier–Stokes computations on unstructured triangular meshes. *AIAA Journal* 1993; **31**(9): 1618–1625.
14. Ethier CR, Steinman DA. Exact fully 3D Navier–Stokes solutions for benchmarking. *International Journal for Numerical Methods in Fluids* 1994; **19**: 369–375.
15. Rudman M. Volume-tracking methods for interfacial flow calculations. *International Journal for Numerical Methods in Fluids* 1997; **24**: 671–691.
16. Li XL, Jin BX, Glimm J. Numerical study for the three-dimensional Rayleigh–Taylor instability through the TVD/AC scheme and parallel computation. *Journal of Computational Physics* 1996; **126**: 343–355.
17. Daly BJ. Numerical study of two fluid Rayleigh–Taylor instability. *Physics of Fluids* 1967; **10**(2): 297–307.
18. Chandrasekhar S. *Hydroynamics and Hydromagnetics Stability*. Oxford University Press: London, 1961; 428–447.
19. Anon. Cooperative experiments on Wigley parabolic models in Japan. In *17th ITTC Resistance Committee Report* (2nd edition). University of Tokyo: Tokyo, Japan; Chapters 3 and 5, 1983.

